

**Maxwell's two-demon engine under pure dephasing noise**Feng-Jui Chan,<sup>1,2,\*</sup> Yi-Te Huang<sup>1,2,\*</sup>, Jhen-Dong Lin,<sup>1,2</sup> Huan-Yu Ku<sup>1,2,3,4</sup>, Jui-Sheng Chen,<sup>1,2</sup>  
Hong-Bin Chen<sup>1,2,5,†</sup> and Yueh-Nan Chen<sup>1,2,‡</sup><sup>1</sup>*Department of Physics, National Cheng Kung University, 701 Tainan, Taiwan*<sup>2</sup>*Center for Quantum Frontiers of Research & Technology (QFort), National Cheng Kung University, 701 Tainan, Taiwan*<sup>3</sup>*Faculty of Physics, University of Vienna, Boltzmannngasse 5, 1090 Vienna, Austria*<sup>4</sup>*Institute for Quantum Optics and Quantum Information (IQOQI), Austrian Academy of Sciences,  
Boltzmannngasse 3, 1090 Vienna, Austria*<sup>5</sup>*Department of Engineering Science, National Cheng Kung University, 701 Tainan, Taiwan*

(Received 8 June 2022; accepted 3 October 2022; published 1 November 2022)

The interplay between thermal machines and quantum correlations is of great interest in both quantum thermodynamics and quantum information science. Recently, a quantum Szilárd engine has been proposed, showing that the quantum steerability between a Maxwell's demon and a work medium can be beneficial to a work extraction task. Nevertheless, this type of quantum-fueled machine is usually fragile in the presence of decoherence effects. Therefore, in this work we tackle this question by introducing a second demon who can access a control system and make the work medium pass through two dephasing channels in a manner of quantum superposition. Furthermore, we provide a quantum circuit to simulate our proposed concept and test it on IBMQ and IonQ quantum computers.

DOI: [10.1103/PhysRevA.106.052201](https://doi.org/10.1103/PhysRevA.106.052201)**I. INTRODUCTION**

Due to the development of quantum theory, the microscopic picture of thermodynamics is constructed by reconciling the quantum phenomena and is turned into a new version called quantum thermodynamics. In fact, it is conceived from the necessity to deal with quantum effects, e.g., quantum superposition and quantum correlations, for different scenarios, such as thermal engine [1–13], protocols for work extractions [9,14–18], and fluctuations of work [19–21]. Recently, quantum steering [22–26], a type of spatial quantum correlations, has been used to demonstrate quantum advantage on a quantum Szilárd engine [27,28], a work extraction machine assisted by Maxwell's demon [29]. A steering-type inequality is derived in terms of classical limit of the engine's work output, i.e., the maximum extractable work by using classical resources. They further show that some steerable resources can exceed this classical limit, implying that the Maxwell's demon should be certified as a genuinely “quantum” entity for these cases.

In contrast to the quantum correlations for spatially separated systems, Leggett and Garg proposed the concept called (non-)macrorealism and the well-known Leggett-Garg inequality [30,31], suggesting that the nonclassical features can also be revealed in temporal evolutions of quantum systems (see Ref. [32] for a comprehensive review). The nonclassical properties in time domain are now termed “temporal quantum correlations,” which are beneficial to several quantum infor-

mation tasks, such as certifying quantum memory [33,34] and self-testing quantum measurement [35].

As aforementioned, Ref. [27] investigated the influence of spatial quantum steerability on a heat engine. Here we propose a mirror of this steering heat engine by considering temporal quantum steering [36–40]. More specifically, in each round of the experiment, the Maxwell's demon (say Alice for convenience) performs a measurement on the work medium taken from a heat bath. She then sends the work medium to Bob through a quantum channel, so that Bob can charge his battery by extracting energy from the work medium. We also derive a temporal steering inequality in terms of the classical limit of the extractable work, which can be numerically computed via semidefinite program (SDP). Therefore we can identify useful temporal steerable resources that can demonstrate a quantum advantage for the work extraction task.

In practice, the quantum channel between Alice and Bob could suffer from unwanted noise that further degrades the temporal steerability as well as the engine's performance. To tackle this problem, we adopt the recent developed scheme called a superposition of quantum channels, which has been utilized in quantum information science [41–48]. This approach involves two or several channels placed in parallel and introduces a control system to decide which channel for the work medium to pass through. We consider that the control system can be accessed by another demon, Charlie. He can prepare the control system in a quantum superposition state so that the work medium can also pass through the channels in a manner of quantum superposition. Before Bob receives the work medium, Charlie can perform a selective measurement on the control system and discard the unwanted results.

In this work we consider a superposition of two pure dephasing channels. With Charlie's assistance, one can observe

\*These authors contributed equally to this work.

†hongbinchen@gs.ncku.edu.tw

‡yuehnan@mail.ncku.edu.tw

an enhancement of the extractable work in comparison with the case that involves only one dephasing channel. Moreover, we implement the two-demon engine on IBMQ and IonQ quantum computers [49–52]. We find that even in the presence of the intrinsic errors of the quantum computers, the results still demonstrate significant enhancement with the help of the superposition of quantum channels and the second demon. To further analyze the effect of the intrinsic errors, we also consider a Markovian noise model to numerically simulate device imperfections. We find that the results for IBMQ are in good agreement with our noise simulations, while those for IonQ contain unexpected oscillatory behavior, suggesting a non-Markovian nature of the device.

## II. SINGLE-DEMON HEAT ENGINE

In this section we provide a detailed description of the work extraction engine with only one Maxwell’s demon (Alice). Also, we derive the temporal steering inequality in terms of the classical limit of the engine’s work output.

Let us start from the process to extract work from a work medium. We consider that the work medium  $\mathcal{W}$  is modeled as a two-level system with the Hamiltonian  $\hat{H}_{\mathcal{W}} = \hbar\omega|1\rangle\langle 1|$ , where  $\hbar\omega$  is the energy difference between the excited state  $|1\rangle$  and the ground state  $|0\rangle$ . In general, a work extraction operation is a process that transfers the energy from a work medium to a battery. As reported in Refs. [15,16], an ideal work extraction process can be described by a local unitary evolution acting on the work medium  $\mathcal{W}$ , because it does not decrease the entropy of  $\mathcal{W}$ . If the quantum state of the work medium is available, one can then design a suitable work extraction operation for this particular state. When the work medium is prepared in a pure state  $|\psi\rangle$ , then the optimal work extraction strategy is described by a local unitary  $U$  such that  $U|\psi\rangle = |0\rangle$ . This idea can be generalized to the situation where the work medium is prepared in a mixed state. A mixed state can be interpreted as a statistical mixture of pure states. In fact, for a given mixed state  $\rho_{\mathcal{W}}$ , there are infinite possibilities of pure state decomposition  $D = \{p_k, |\psi_k\rangle\langle\psi_k|\}$  such that  $\sum_k p_k |\psi_k\rangle\langle\psi_k| = \rho_{\mathcal{W}}$ . If a Maxwell’s demon can reveal the knowledge of this decomposition, one can then design a set of optimal work extraction operations  $\{U_k\}$ . Therefore the average extracted work can be expressed as  $\bar{W} = \sum_k p_k \Delta W_k$ , where

$$\Delta W_k = \text{Tr}[\hat{H}_{\mathcal{W}}|\psi_k\rangle\langle\psi_k|] - \text{Tr}[\hat{H}_{\mathcal{W}}U_k|\psi_k\rangle\langle\psi_k|U_k^\dagger]. \quad (1)$$

Now we introduce the single-demon heat engine, as shown in Fig. 1. A thermal bath can supply unlimited copies of work medium  $\mathcal{W}$ , which is initialized in the Gibbs state at temperature  $T$ . Alice (the demon) performs a measurement (labeled by  $x$ ) on  $\mathcal{W}$  with the associated outcome (labeled by  $a$ ). The work medium with the postmeasurement state  $\rho_{a|x}$  is then sent to Bob via a noisy quantum channel  $\Lambda$ . In addition, Alice informs Bob of  $(a, x)$  through a classical communication so that Bob can apply a unitary operator  $U_{a|x}$  to  $\mathcal{W}$  to extract work according to Alice’s message. Thus the extracted work for the measurement  $x$  with the outcome  $a$  is given by

$$\Delta W_{a|x} = \text{Tr}[\hat{H}_{\mathcal{W}}\Lambda(\rho_{a|x})] - \text{Tr}[\hat{H}_{\mathcal{W}}U_{a|x}\Lambda(\rho_{a|x})U_{a|x}^\dagger]. \quad (2)$$

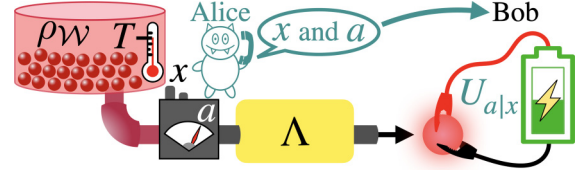


FIG. 1. Schematic illustration of the single-demon heat engine. Alice (a Maxwell’s demon) takes a work medium  $\mathcal{W}$  from a thermal bath at temperature  $T$ . She then performs a measurement labeled by  $x$  and obtains the corresponding outcome  $a$ . Then Alice informs Bob of  $(a, x)$  through a classical communication and sends the post-measurement work medium through a pure dephasing channel  $\Lambda$  to Bob. After that, Bob chooses a suitable work extraction operation  $U_{a|x}$  based on Alice’s information.

The average extracted work can then be expressed as

$$\begin{aligned} \bar{W}_{\Lambda} &= \sum_{a,x} p(x)p(a|x)\Delta W_{a|x} \\ &= \sum_{a,x} \text{Tr}[p(a|x)F_{a|x}\Lambda(\rho_{a|x})], \end{aligned} \quad (3)$$

where the shorthand  $F_{a|x} := p(x)(\hat{H}_{\mathcal{W}} - U_{a|x}^\dagger \hat{H}_{\mathcal{W}} U_{a|x})$  is adopted for convenience,  $p(x)$  is the probability of Alice’s choice on measurements, and  $p(a|x)$  is the probability of obtaining the outcome  $a$  conditioned on the measurement  $x$ . The work extraction unitaries  $\{U_{a|x}\}_{a,x}$  can be optimized for the postmeasurement states  $\{\rho_{a|x}\}_{a,x}$ , i.e.,  $U_{a|x}\rho_{a|x}U_{a|x}^\dagger = |0\rangle\langle 0|$  for all  $a$  and  $x$ . However, the presence of the noise in the quantum channel  $\Lambda$  invalidates the optimal extraction process; consequently, the average extracted work will be impaired due to the noise. Note that the average extracted work  $\bar{W}_{\Lambda}$  can be regarded as a linear function of the so-called temporal steering assemblage  $\{p(a|x)\Lambda(\rho_{a|x})\}_{a,x}$ , which is a widely accepted terminology for characterizing one-sided device-independent nature of steering scenarios [53–56]. In other words, one can relax the assumptions of Alice’s measurement devices.

Let us now present a concrete example. In each round of the work extraction task, Alice receives a work medium in the Gibbs state at the infinite temperature, i.e.,  $\rho_{\mathcal{W}} = \mathbb{1}/2$ , from the bath and randomly performs one of the two measurements  $\sigma_z = |0\rangle\langle 0| - |1\rangle\langle 1|$  or  $\sigma_x = |0\rangle\langle 1| + |1\rangle\langle 0|$  on  $\mathcal{W}$  with equal probability. She then sends the  $\mathcal{W}$  with the postmeasurement state  $\rho_{a|x}$  to Bob through a pure dephasing channel  $\Lambda$  described by

$$\Lambda(\rho) = \left(1 - \frac{\gamma}{2}\right)\rho + \frac{\gamma}{2}\sigma_z\rho\sigma_z, \quad (4)$$

where  $\gamma$  denotes the dephasing strength. In addition, she informs him of the message  $(a, x)$  via a classical communication. After receiving the message, Bob then applies  $U_{a|x}$  to the work medium  $\mathcal{W}$ . The corresponding  $U_{a|x}$ ,  $F_{a|x}$ , and the measurement settings are summarized in Table I. For this setting, the average extracted work is given by

$$\bar{W}_{\Lambda} = \frac{2-\gamma}{4} \hbar\omega. \quad (5)$$

As expected, the average extracted work decreases monotonically when the dephasing strength  $\gamma$  increases. We note that, since  $\Lambda$  is Gibbs preserving [57–61], it does not change

TABLE I. A list of Alice's measurement results,  $p(a|x)$  and  $\rho_{a|x}$ , and the work extraction procedure (described by  $U_{a|x}$  and  $F_{a|x}$ ) on Bob's side. Here,  $|\pm\rangle = (|0\rangle \pm |1\rangle)/\sqrt{2}$ ,  $\sigma_z = |0\rangle\langle 0| - |1\rangle\langle 1|$ ,  $\sigma_x = |0\rangle\langle 1| + |1\rangle\langle 0|$ , and  $H = (\sigma_z + \sigma_x)/\sqrt{2}$  denotes the Hadamard transform.

| $x$          | $\sigma_z$            |                                  | $\sigma_x$                                    |   |
|--------------|-----------------------|----------------------------------|---|---|
|              | +1                    | -1                               | +1  | -1  |
| $p(x)$       | 0.5                   |                                  | 0.5   |   |
| $a$          | +1                    | -1                               | +1  | -1  |
| $p(a x)$     | 0.5                   | 0.5                              | 0.5   | 0.5   |
| $U_{a x}$    | $\mathbb{1}$          | $\sigma_x$                       | $H$   | $\sigma_x H$                                  |
| $\rho_{a x}$ | $ 0\rangle\langle 0 $ | $ 1\rangle\langle 1 $            | $ +\rangle\langle + $                         | $ -\rangle\langle - $                         |
| $F_{a x}$    | 0                     | $-\frac{\hbar\omega}{2}\sigma_z$ | $-\frac{\hbar\omega}{4}(\sigma_z - \sigma_x)$ | $-\frac{\hbar\omega}{4}(\sigma_z + \sigma_x)$ |

the thermal state of  $\mathcal{W}$  on average. Thus, the work medium remains the same Gibbs state on average after the delivery, i.e.,  $\sum_a p(a|x)\Lambda(\rho_{a|x}) = \rho_{\mathcal{W}}$  for all  $x$ .

Let us turn to the description of classical strategy. In classical world one can perform noninvasive measurement to reveal physical properties of a system without disturbing its state and its consequent dynamics [30]. Suppose that there exists a hidden variable  $\lambda$  associated with a classical randomness  $p(\lambda)$ , and for each moment the work medium  $\mathcal{W}$  is described by a predetermined hidden state  $\rho_\lambda$ . If Alice performs noninvasive measurements, where she only reveals the hidden variable  $\lambda$  without changing the state of  $\mathcal{W}$ , her measurements can be described by a classical postprocessing  $p(a|x, \lambda)$ . In this case the temporal steering assemblage received by Bob can be described by a hidden state (HS) model, i.e.,

$$\sigma_{a|x}^{\text{HS}} = \sum_{\lambda} p(\lambda) p(a|x, \lambda) \rho_{\lambda} \quad \forall a, x. \quad (6)$$

Therefore, given a work extraction protocol, which is described by  $\{F_{a|x}\}_{a|x}$  and the Gibbs state  $\rho_{\mathcal{W}}$ , the maximal value of the average extracted work attainable by classical assemblages is given by

$$\begin{aligned} \bar{W}_{\text{cl}} &= \max_{\{\tilde{\sigma}_{a|x}\} \in \mathcal{C}} \sum_{a,x} \text{Tr}[F_{a|x} \tilde{\sigma}_{a|x}], \\ \text{s.t. } \sum_a \tilde{\sigma}_{a|x} &= \rho_{\mathcal{W}} \quad \forall x, \end{aligned} \quad (7)$$

where  $\mathcal{C}$  denotes the set of all HS models. The constraint in the second line of Eq. (7) is introduced because the HS model should also preserve the same Gibbs state on average. Moreover, Eq. (7) can be considered as a convex optimization problem, because  $\mathcal{C}$  is a convex set. In Appendix A we show that one can recast the classical limit of average extracted work in Eq. (7) as a semidefinite program (SDP), which can be solved numerically [62]. Therefore, when a temporal steerable resource can exceed this classical limit, i.e.,  $\bar{W}_{\Lambda} \geq \bar{W}_{\text{cl}}$ , Bob can be convinced that Alice is a genuinely "quantum" Maxwell's demon.

For the aforementioned concrete example, as summarized in Table I, the classical limit of the  $\bar{W}$  is

$$\bar{W}_{\text{cl}} \approx 0.354 \hbar\omega \quad (8)$$

(see also Appendix A for the optimal solution of HS model in this case). Note that the above classical limit can be violated

if  $\gamma < \gamma_{\text{TH}} \approx 0.586$ , where  $\gamma_{\text{TH}}$  is the quantum-to-classical transition threshold for the dephasing channel in Eq. (4).

It is worthwhile to note that the SDP method presented in Appendix A can obtain the same values of the classical limit in the cases proposed in Refs. [27,28]. Nevertheless, their derivations only work for restricted considerations of  $p(x)$  as well as the numbers of measurements  $x$  and outcomes  $a$ . Here we generalize their considerations by providing an efficient approach to compute the value of classical limit in arbitrary work extraction tasks.

Further, in comparison with the standard steering inequality (see Ref. [25], for instance), the classical limit  $\bar{W}_{\text{cl}}$  in Eq. (7) endows the mathematical hyperplane theory with a physical interpretation in a thermodynamical fashion. Thus  $\bar{W}_{\text{cl}}$  can be seen as a thermodynamical temporal steering witness. However, the thermodynamical steering witness cannot certify all steerable resources because the constitution of the Hamiltonian and the unitary cannot in general represent all positive semidefinite operators, which is used to construct a steering witness.

### III. TWO-DEMON HEAT ENGINE

We have shown the detrimental effects of the noise in the quantum channel  $\Lambda$  on the work extraction task. To quench the noise in  $\Lambda$  requires substantial efforts, which are typically formidable obstacles in various branches of quantum technology. Instead of tackling the noise by engineering the quantum channel  $\Lambda$ , we circumvent this obstacle by the approach of the superposition of quantum channels, as shown in Fig. 2.

More specifically, instead of a single quantum channel  $\Lambda$ , we consider a superposition of two channels, which involves an additional control system  $C$  that can be accessed by the second demon, Charlie. The state of  $C$  determines which

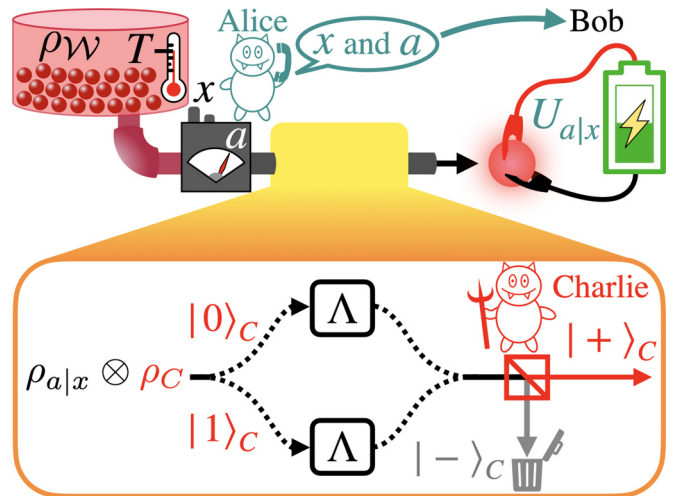


FIG. 2. Schematic illustration of the two-demon heat engine. The second demon, Charlie, can prepare a state of control system  $\rho_C$  to determine which of the two channels the work medium to pass through and perform a selective measurement on the control system. If the control system is prepared in a superposition state, the work medium can pass through two dephasing channels in a manner of superposition.

channel for  $\mathcal{W}$  to pass through. Charlie also performs a selective measurement on  $C$  to condition the dynamics of the work medium before reaching Bob. In the following we will show that if the control system is prepared in a superposition state, one can observe a clear enhancement of the average extracted work compared with the case of the single use of the dephasing channel discussed in the previous section.

Before elaborating the superposition of quantum channels [43], it will be helpful to specify the implementation of a single quantum channel. According to the Stinespring dilation theorem [63–65], any channel with Kraus operators  $\{K_k\}_k$  can be implemented by a unitary  $V_{\mathcal{W},E}$  acting on the work medium  $\mathcal{W}$  and an environment  $E$ . For the dephasing channel Eq. (4), it can be implemented by the following  $V_{\mathcal{W},E}$ :

$$\begin{aligned} V_{\mathcal{W},E}|0\rangle_{\mathcal{W}}|0\rangle_E &= \sqrt{1-\frac{\gamma}{2}}|0\rangle_{\mathcal{W}}|0\rangle_E - i\sqrt{\frac{\gamma}{2}}|0\rangle_{\mathcal{W}}|1\rangle_E, \\ V_{\mathcal{W},E}|1\rangle_{\mathcal{W}}|0\rangle_E &= \sqrt{1-\frac{\gamma}{2}}|1\rangle_{\mathcal{W}}|0\rangle_E + i\sqrt{\frac{\gamma}{2}}|1\rangle_{\mathcal{W}}|1\rangle_E. \end{aligned} \quad (9)$$

If  $E$  is initialized in the state  $|0\rangle_E$ , the corresponding Kraus operators are  $K_0 = \sqrt{1-\gamma/2} \mathbb{1}$  and  $K_1 = -i\sqrt{\gamma/2} \sigma_z$ .

To implement the superposition of two quantum channels, we introduce two independent environments,  $E_0$  and  $E_1$ , giving rise to the two channels to be superposed. Along with a control qubit  $C$ , Charlie can determine which environment to interact with according to the state of  $C$  by the global unitary:

$$V_T = |0\rangle\langle 0|_C \otimes V_{\mathcal{W},E_0} + |1\rangle\langle 1|_C \otimes V_{\mathcal{W},E_1}. \quad (10)$$

Particularly, if  $C$  is prepared in a superposition state  $|+\rangle_C = (|0\rangle_C + |1\rangle_C)/\sqrt{2}$ ,  $\mathcal{W}$  can pass through the two channels in a manner of quantum superposition. Then the joint state of  $C$  and  $\mathcal{W}$  evolves according to

$$\begin{aligned} \rho_{C\mathcal{W}} &= \text{Tr}_{E_0,E_1}[V_T(|+\rangle\langle +|_C \otimes \rho \otimes |0\rangle\langle 0|_{E_0} \otimes |0\rangle\langle 0|_{E_1})V_T^\dagger] \\ &= \frac{1}{2}[\mathbb{1} \otimes \Lambda(\rho) + \sigma_x \otimes K_0\rho K_0^\dagger]. \end{aligned} \quad (11)$$

Before sending  $\mathcal{W}$  to Bob, Charlie will perform a selective measurement on  $C$ . For a concrete example, we assume that Charlie measures the observable  $\sigma_x$  on  $C$  and only selects the outcome associated with the eigenstate  $|+\rangle_C$ , while the one associated with the eigenstate  $|-\rangle_C$  is discarded. The normalized postmeasurement state of  $\mathcal{W}$  is given by

$$\mathcal{S}(\rho) = \frac{\Lambda_+(\rho)}{\text{Tr}[\Lambda_+(\rho)]}, \quad (12)$$

where

$$\begin{aligned} \Lambda_+(\rho) &= \text{Tr}_C[(|+\rangle\langle +| \otimes \mathbb{1})\rho_{C\mathcal{W}}(|+\rangle\langle +| \otimes \mathbb{1})^\dagger] \\ &= \frac{1}{2}[\Lambda(\rho) + K_0\rho K_0^\dagger]. \end{aligned} \quad (13)$$

Note that Eq. (12) is in general a nonlinear equation. Nevertheless,  $\mathcal{S}(\rho)$  is still a linear process in this case because  $\text{Tr}[\Lambda_+(\rho)] = 1 - \gamma/4$  for arbitrary input state  $\rho$ . We refer the reader to see Refs. [66–69] when the most general cases are considered. Therefore the effective evolution of  $\mathcal{W}$  under the superposition scenario can be written as

$$\mathcal{S}(\rho) = \left(1 - \frac{\gamma'}{2}\right)\rho + \frac{\gamma'}{2}\sigma_z\rho\sigma_z, \quad (14)$$

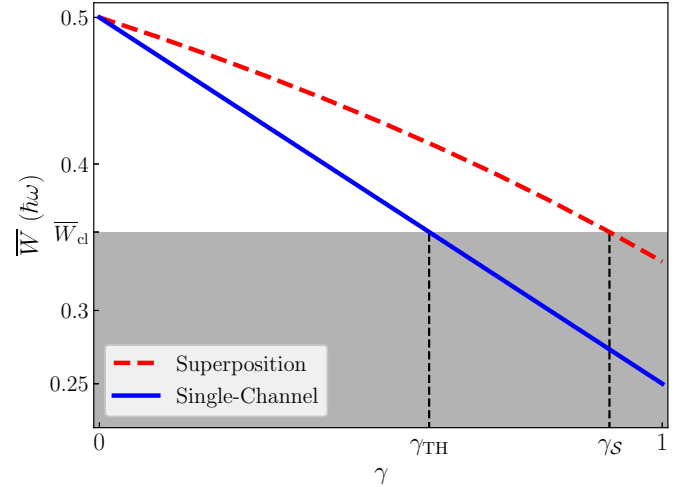


FIG. 3. The average extracted works for pure dephasing channels. The blue solid line and red dashed line represent the  $\bar{W}$  obtained from a single-channel and superposition scenario, respectively. One can observe that the average extracted work can be enhanced when the second demon (Charlie) superposes two dephasing channels, i.e.,  $\bar{W}_S \geq \bar{W}_\Lambda$ . Here,  $\gamma_{\text{TH}} \approx 0.586$  and  $\gamma_S \approx 0.906$  are the quantum-to-classical transition thresholds.

where  $\gamma' = 2\gamma/(4-\gamma)$ . It is crucial to note that the overall effect of the superposition of two pure dephasing channels is equivalent to a single pure dephasing channel with dephasing strength  $\gamma' \leq \gamma$ , for  $0 \leq \gamma \leq 1$ . Therefore the effect of the noise in a single channel is quenched.

Finally, we apply this approach to the work extraction task, and the average extracted work in this case reads

$$\begin{aligned} \bar{W}_S &= \sum_{a,x} \text{Tr}[p(a|x)F_{a|x}\mathcal{S}(\rho_{a|x})] \\ &= \frac{2-\gamma'}{4} \hbar\omega. \end{aligned} \quad (15)$$

The transition threshold in this case is given by  $\gamma_S \approx 0.906$ . The comparison of the average extracted works between a single-channel and superposition scenario is presented in Fig. 3. One clearly sees that  $\bar{W}_S \geq \bar{W}_\Lambda$  for  $\gamma \in [0, 1]$ . Note that if Charlie does not perform the measurement on the control system  $C$ , i.e.,  $\mathcal{S}(\rho) = \text{Tr}_C[\rho_{C\mathcal{W}}] = \Lambda(\rho)$ , one can observe that  $\bar{W}_S = \bar{W}_\Lambda$ . This means that the operation conducted by the second demon, Charlie, is essential for enhancing the extracted work.

#### IV. CIRCUIT REALIZATIONS AND NOISE SIMULATIONS

In this section we provide a circuit model for the two-demon heat engine with the superposition of two pure dephasing channels. In addition, we implement the circuit on IBMQ and IonQ quantum computers, where the enhancement due to the second demon, Charlie, can be clearly observed. Moreover, we introduce the noise simulation algorithm and compare the results from IBMQ and IonQ devices with the noise simulations.

The circuit model consists of four qubits: the control  $C$ , the work medium  $\mathcal{W}$ , and the environments,  $E_0$  and  $E_1$ . The

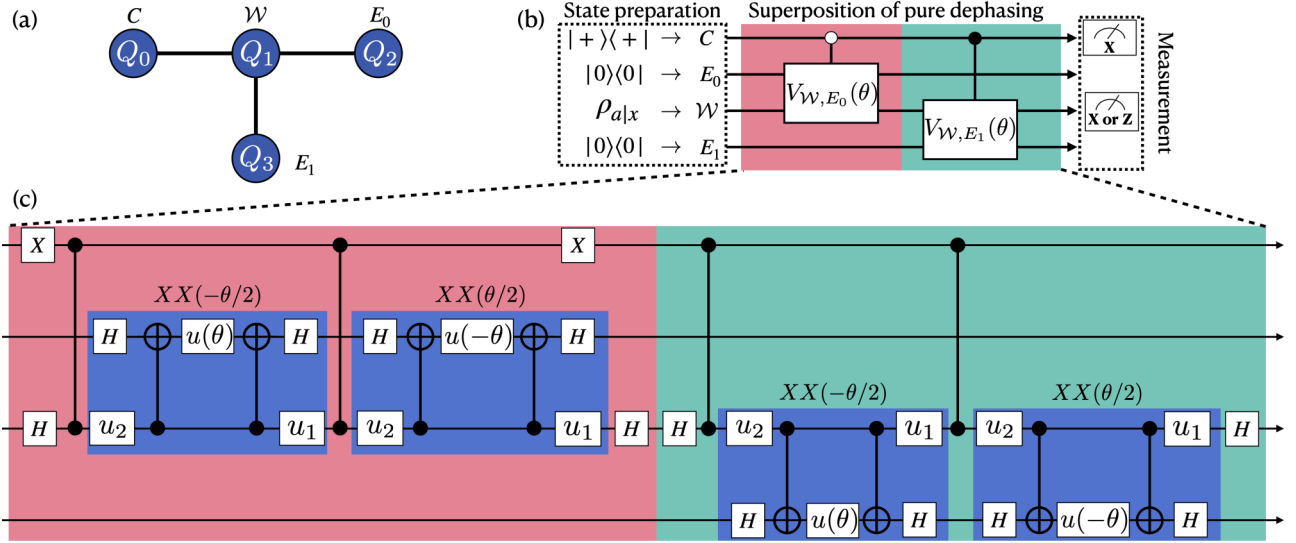


FIG. 4. (a) The qubits we choose in *ibmq\_jakarta* and the corresponding coupling map. Here  $Q_0$ ,  $Q_1$ ,  $Q_2$ , and  $Q_3$  serve as  $C$ ,  $\mathcal{W}$ ,  $E_0$ , and  $E_1$ , respectively. (b) Circuit model for the temporal steering heat engine with superposition of dephasing channels. (c) The gate sequence for implementing the superposition of pure dephasing channels. Here  $u_1$ ,  $u_2$ , and  $u(\theta)$  are given by Eq. (16).

connections between qubits and the labels on IBMQ device are shown in Fig. 4(a). On the other hand, due to the full connectivity of the trapped ion device, we can choose four arbitrary qubits on IonQ device for the circuit. The circuit model is described in Fig. 4(b) and can be divided into three parts: (1) state preparation, (2) superposition of pure dephasing channels, and (3) measurements on  $C$  and  $\mathcal{W}$ . In part 1, we prepare the control system  $C$  and the environments in  $|+\rangle|+\rangle$  and  $|0\rangle|0\rangle$ , respectively. Also, we replace Alice's measurements by directly preparing the postmeasurement state  $\rho_{a|x}$  in Table I and assign the probability  $p(a|x) = 1/2 \forall a, x$ .

In part 2, we construct the  $V_{\mathcal{W}, E}(\theta)$  according to Eq. (9), and the dephasing strength is modulated through the rotation angle  $\theta$  with  $\theta = \arccos(1 - \gamma)$ . In addition, to achieve the superposition of quantum channels, we make a series of controlled unitaries according to Eq. (10). As shown in Fig. 4(c) (see also Appendix B for details), each controlled unitary can be decomposed into two controlled-Z gates and two Ising coupling gates  $XX(\theta) = \cos \theta/2 \mathbb{1} \otimes \mathbb{1} - i \sin \theta/2 \sigma_x \otimes \sigma_x$ . Note that,  $XX(\theta)$  is a native gate for the IonQ trapped ion quantum computer. Nevertheless, because the Ising coupling gate is not a native gate in IBMQ, we further decompose the  $XX$  gate into CNOT gates,  $H$  gates, and three other single-qubit gates listed as follows:

$$u_1 = \frac{1}{\sqrt{2}} \begin{pmatrix} 1 & -i \\ -1 & -i \end{pmatrix}, \quad u_2 = \frac{1}{\sqrt{2}} \begin{pmatrix} 1 & -1 \\ i & i \end{pmatrix},$$

$$u(\theta) = \text{diag}(1, e^{i\theta/2}). \quad (16)$$

Note that  $u_1 = U3(\pi/2, \pi, \pi/2)$ ,  $u_2 = U3(\pi/2, \pi/2, 0)$ , and  $u(\theta) = P(\theta/2)$  can be easily implemented in IBMQ, where

$$P(\theta) = \begin{pmatrix} 1 & 0 \\ 0 & e^{i\theta} \end{pmatrix}$$

$$\text{and } U3(\theta, \phi, \xi) = \begin{pmatrix} \cos(\frac{\theta}{2}) & -e^{i\xi} \sin(\frac{\theta}{2}) \\ e^{i\phi} \sin(\frac{\theta}{2}) & e^{i(\phi+\xi)} \cos(\frac{\theta}{2}) \end{pmatrix}. \quad (17)$$

In part 3 we measure  $C$  in the  $\sigma_x$  basis and denote 0 (1) as the outcome associated with the eigenstate  $|+\rangle_C$  ( $|-\rangle_C$ ). For the single-channel scenario, both of the outcomes are taken into account, whereas for the superposition scenario, we postselect the outcome 0. Furthermore, as indicated in Eq. (3), the average extracted work can be obtained by the expectation values  $\{\langle F_{a|x} \rangle = \text{Tr}(F_{a|x} \rho_{a|x})\}_{a,x}$ . In addition, as summarized in Table I, each  $\langle F_{a|x} \rangle$  can be constructed by  $\{\langle \sigma_i \rangle_{a|x} = \text{Tr}(\sigma_i \rho_{a|x})\}_{i \in \{x,z\}}$ . Therefore, instead of applying the work extraction unitaries  $\{U_{a|x}\}$ , we measure the observables  $\sigma_x$  and  $\sigma_z$  on  $\mathcal{W}$  to estimate  $\bar{W}_\Lambda$  and  $\bar{W}_S$ .

In Fig. 5 we present the results obtained from the devices of *ibmq\_jakarta* and IonQ. For each circuit, it runs with 8192 shots and 1000 shots for IBMQ and IonQ devices, respectively. The blue dots and the red triangles represent the average extracted work for the scenarios with and without the postselection, respectively. We can observe a clear enhancement due to the postselection.

To gain a further insight on the devices' imperfections, we perform noise simulations [70,71] (the solid and dashed curves in Fig. 5) that take the intrinsic errors of the quantum devices into account. To model the intrinsic errors, we consider three major sources of the errors, including the qubit relaxation, the qubit decoherence, the two-qubit gate error, and the readout error. The corresponding relaxation rate ( $\eta_{T1}$ ), decoherence rate ( $\eta_{T2}$ ), and the error rates of the devices, *ibmq\_jakarta* and IonQ, are summarized in Tables II and III. In the following, we elaborate on the noise model in detail.

The qubit relaxation and decoherence are described by the following Lindblad master equation:

$$\dot{\rho}(t) := \mathcal{L}[\rho(t)]$$

$$= \frac{\eta_{T1}}{2} [2\sigma_- \rho(t) \sigma_+ - \sigma_+ \sigma_- \rho(t) - \rho(t) \sigma_+ \sigma_-]$$

$$+ \eta_{T2} [\sigma_z \rho(t) \sigma_z - \rho(t)]. \quad (18)$$

TABLE II. A summary of the intrinsic errors for the *ibmq\_jakarta* and IonQ devices, which include the qubit relaxation rate  $\eta_{T_1}$ , decoherence rate  $\eta_{T_2}$ , and readout error rate  $\Gamma$ . The gate times for single-qubit gates are also presented in the table.

|      | Qubit | $\eta_{T_1}(\text{ns}^{-1})$ | $\eta_{T_2}(\text{ns}^{-1})$ | Single-qubit gate time (ns) | $\Gamma$ |
|------|-------|------------------------------|------------------------------|-----------------------------|----------|
| IBMQ | $Q_0$ | $6.35 \times 10^{-6}$        | $1.45 \times 10^{-5}$        | 35.56                       | 1.95%    |
|      | $Q_1$ | $7.62 \times 10^{-6}$        | $2.78 \times 10^{-5}$        | 35.56                       | 2.12%    |
|      | $Q_2$ | $6.94 \times 10^{-6}$        | $2.01 \times 10^{-5}$        | 35.56                       | N/A      |
|      | $Q_3$ | $1.02 \times 10^{-5}$        | $1.44 \times 10^{-5}$        | 35.56                       | N/A      |
| IonQ | All   | $10^{-10}$                   | $2.48 \times 10^{-9}$        | $10^4$                      | 0.39%    |

When each ideal quantum gate (or unitary transformation) is applied to the system, we apply the propagation of the state according to Eq. (18), i.e.,  $\exp(\mathcal{L}t)$ , where  $t$  is the gate time.

Among the gates we implement, two-qubit gates are the major source of gate errors because their gate time is almost one order of magnitude longer than that of single-qubit gates. Following the idea from Refs. [72–74], we model the gate error as a depolarizing channel denoted as

$$\mathcal{G}_{\text{cr}}(\rho) = (1 - p_{\text{GE}})\rho + p_{\text{GE}}\frac{\mathbb{1}}{2}, \quad (19)$$

where  $p_{\text{GE}}$  is the two-qubit gate error rate. We apply the model after the Lindblad master equation only when a two-qubit gate is operated on the circuit.

To model the readout errors, we recall that quantum computers measure the systems in a computational basis,  $|0\rangle$  and  $|1\rangle$ . The outcome is 0 (1) when the qubit is in  $|0\rangle$  ( $|1\rangle$ ) in the ideal case. Hence we can determine the readout error rate  $\Gamma$  by the average probability of measuring  $|0\rangle$  ( $|1\rangle$ ) but obtaining the opposite outcome 1 (0). Therefore the readout errors can be modeled as a bit-flip channel, i.e.,

$$\mathcal{E}_{\text{readout}}(\rho) = (1 - \Gamma)\rho + \Gamma \sigma_x \rho \sigma_x. \quad (20)$$

Here we give a brief summary of our noise simulation process and how this is integrated with the superposition scenario in Sec. III. We first modulate the dephasing strength  $\gamma$  through the rotation angle  $\theta$  with  $\theta = \arccos(1 - \gamma)$  and provide a circuit model [as shown in Fig. 4(c)] for the superposition scenario in Sec. III. Thus, in order to obtain the average extracted work for a specific  $\gamma$  through the circuit model, one needs to generate totally six quantum circuits because of the four different state preparations and two different measurement observables as presented in Table I. For each quantum circuit, one can apply the noise simulation by considering the intrinsic

TABLE III. A summary of the two-qubit gate time and two-qubit gate error  $p_{\text{GE}}$  for the *ibmq\_jakarta* and IonQ devices. The CNOT (CN) gate is the two-qubit gate for IBMQ devices, and the subscripts represent the qubit indices [see Fig. 4(a)] to which the CN gates are applied. The Ising coupling gate (XX) is the two-qubit gate for IonQ devices. In addition, due to the full connectivity of the trapped ion device, we can apply the XX gate to two arbitrary qubits.

|      | Gate              | Two-qubit gate time (ns) | $p_{\text{GE}}$ |
|------|-------------------|--------------------------|-----------------|
| IBMQ | CN <sub>0,1</sub> | 234.67                   | 0.67%           |
|      | CN <sub>1,2</sub> | 284.44                   | 0.12%           |
|      | CN <sub>1,3</sub> | 384.00                   | 0.8%            |
| IonQ | XX                | $2.1 \times 10^5$        | 3.04%           |

errors (as presented in Tables II and III) including the qubit relaxation and decoherence in Eq. (18), the two-qubit gate error in Eq. (19), and the measurement error in Eq. (20). The noise simulation algorithm for a given quantum circuit can be summarized by the flowchart presented in Fig. 6. As shown in Fig. 5, one can observe that the results from the IBMQ agree with the noise model. However, the results from IonQ do not fit the simulations well. The result at  $\gamma = 0$  is nearly the same as the ideal result, instead of that from noise simulations. It is because the IonQ software provides compulsorily optimized gates, and the total unitary of the circuit at  $\gamma = 0$  is effectively the same as  $\mathbb{1}$  applied to four qubits.

In order to better understand how each intrinsic error affects the work medium and, in particular, the value of average extracted work  $\overline{W}$ , we simplify the discussion by only considering the errors on the work medium ( $Q_1$ ) and taking dephasing strength  $\gamma = 0$  under a single-channel scenario as an example. We first discuss the effect of single-qubit relaxation and decoherence errors on the work medium. As shown in Fig. 4(c), the circuit has totally 26 (6) single-qubit gates and 12 (8) two-qubit gates in IBMQ (IonQ) device. Because the controlled-Z operation is further decomposed into one CNOT gate and two Hadamard gates, one can then estimate the total gate time for IBMQ and IonQ devices are approximately  $4.82 \times 10^3$  and  $1.98 \times 10^6$  ns, respectively. By solving Eq. (18), one can further calculate  $\overline{W}$  by only considering the qubit relaxation and decoherence error on the work medium ( $Q_1$ ). The values obtained for IBMQ and IonQ devices are approximately  $0.4107\hbar\omega$  and  $0.4974\hbar\omega$ , respectively. In this case, the ideal value of  $\overline{W}$  is  $0.5\hbar\omega$ , and one can thus define the error rate of qubit relaxation and decoherence for both devices, namely,  $p_{T_1, T_2}^{\text{IBMQ}} = 17.86\%$  and  $p_{T_1, T_2}^{\text{IonQ}} = 0.52\%$ . Next we discuss the influence of the two-qubit gate error on both devices. For the IonQ device, since there are eight two-qubit gates applied to the work medium  $Q_1$  in total, the effective two-qubit gate error rate for the IonQ device is given as  $p_{\text{GE}}^{\text{IonQ}} = 1 - (1 - 3.04\%)^8 \approx 21.88\%$ . For the IBMQ device, since each CNOT gate (CN<sub>0,1</sub>, CN<sub>1,2</sub>, and CN<sub>1,3</sub>) is applied four times to the work medium  $Q_1$ , the effectively two-qubit gate error rate for the IBMQ device can be given as  $p_{\text{GE}}^{\text{IBMQ}} = 1 - [(1 - 0.67\%)(1 - 0.12\%)(1 - 0.8\%)]^4 \approx 6.18\%$ . Combining all the error rates including qubit relaxation, qubit decoherence, two-qubit gate, and readout, the total error rates for IBMQ and IonQ devices are given by

$$1 - (1 - p_{T_1, T_2}^{\text{IBMQ}})(1 - p_{\text{GE}}^{\text{IBMQ}})(1 - \Gamma_{Q_1}^{\text{IBMQ}}) \approx 24.57\%$$

$$\text{and } 1 - (1 - p_{T_1, T_2}^{\text{IonQ}})(1 - p_{\text{GE}}^{\text{IonQ}})(1 - \Gamma^{\text{IonQ}}) \approx 22.59\%,$$

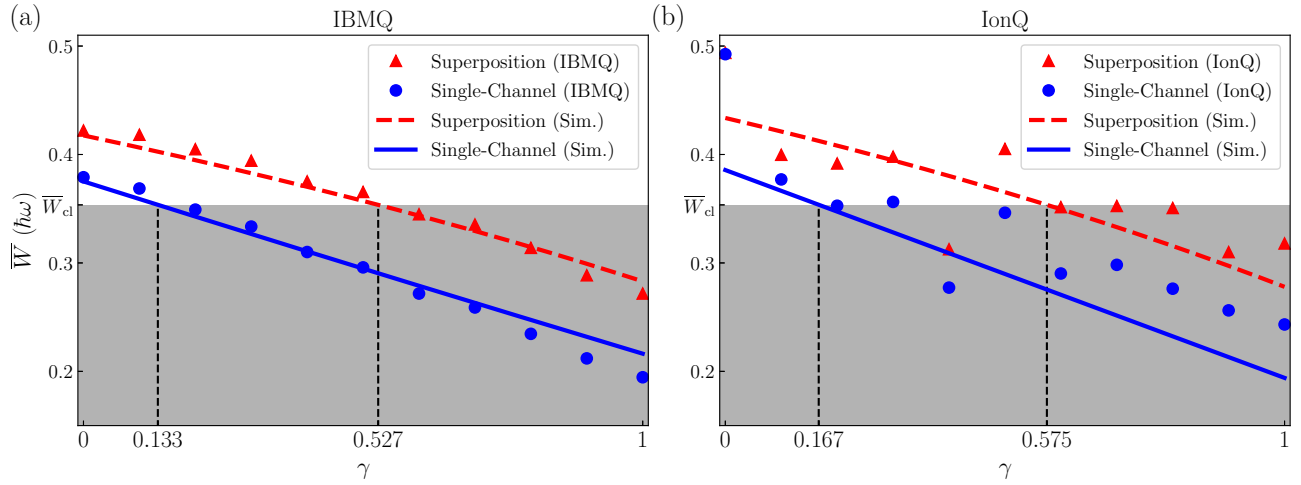


FIG. 5. The noise simulations and results from (a) IBMQ and (b) IonQ devices. The results for  $\bar{W}_\Lambda$  and  $\bar{W}_S$  are represented by blue dots and red triangles, respectively. The corresponding noise simulations are represented by blue-solid and red-dashed curves. Both the noise simulations and results from the devices show that  $\bar{W}_S > \bar{W}_\Lambda$ . (a) For IBMQ, the results fit the noise simulations well. The results from the noise simulations show that  $\bar{W}_S$  and  $\bar{W}_\Lambda$  reach the classical limit  $\bar{W}_{cl}$  at  $\gamma \approx 0.133$  and  $\gamma \approx 0.527$ , respectively. (b) For IonQ, the results show an oscillatory deviation from the noise simulations because of the non-Markovian nature of the device's intrinsic errors. In addition,  $\bar{W}_S$  ( $\bar{W}_\Lambda$ ) obtained from IonQ reaches the classical limit  $\bar{W}_{cl}$  at  $\gamma \approx 0.167$  ( $\gamma \approx 0.575$ ) and are both larger than those from IBMQ.

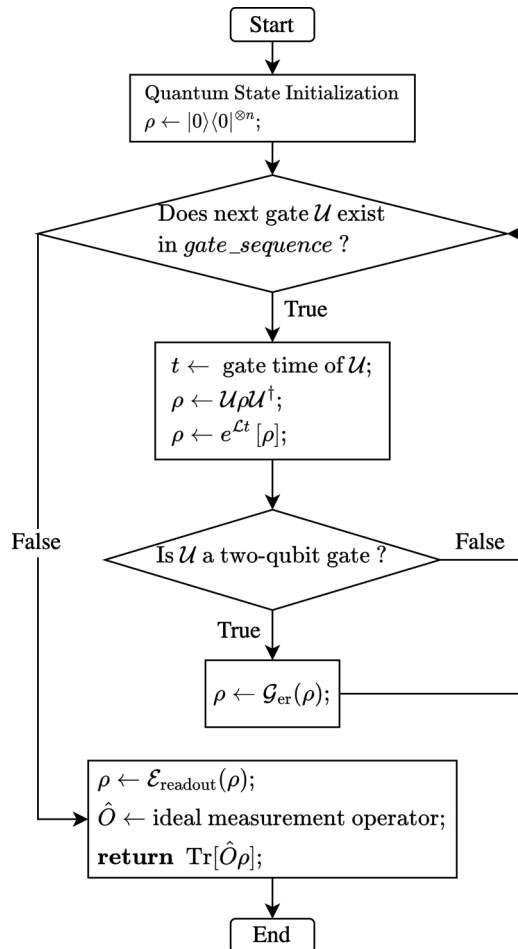


FIG. 6. The flowchart of the noise simulation algorithm for a given  $n$ -qubit quantum circuit with a specific  $gate\_sequence$ .

respectively. As seen, the total error rates for both devices are quite similar, which can also be observed from Fig. 5 (the noise simulation for  $\gamma = 0$  under a single-channel scenario). Note that, for real noise simulation, one has to further take the errors on the other three qubits ( $Q_0$ ,  $Q_2$ , and  $Q_3$ ) into account.

The oscillations of the results obtained from IonQ device, as shown in Fig. 5(b), could originate from the non-Markovian nature of the device's intrinsic errors. More specifically, in our noise simulations, we implicitly assume that the errors of each gate are independent of each other (i.e., the model respects Markov approximation). That is, for the circuits with the same depth (e.g., the circuit model for different dephasing strength  $\gamma$ ), the differences between the ideal results and the noise simulations are roughly the same. Therefore, we do not observe oscillations from the noise simulations in Fig. 5(b); the oscillations observed from the data in Fig. 5(b) suggest that there could be some non-Markovian effects from the intrinsic errors in the IonQ device. For instance, as reported in Ref. [75], the noise of each gate could be correlated and induces the non-Markovian effects.

## V. CONCLUSION

In this work we introduced the notion of a two-demon steering heat engine and obtained the corresponding classical limit for extractable work via SDP. We considered that the work medium passes through a pure dephasing channel. We observed a monotonic decrease of the extractable work and a threshold for quantum-to-classical transition. Further, we utilized a superposition of the pure dephasing channels and introduced the second demon. We can observe clear enhancements of the extractable work and the quantum-to-classical thresholds. Moreover, we performed proof-of-principle demonstrations on IBMQ and IonQ quantum computers. The results

also demonstrate enhancements with the assistance of the second demon, Charlie. The results from IBMQ also agree with the noise simulations that include the accumulation of errors (qubit relaxation, qubit decoherence, two-qubit gate error, and readout error) during the process. On the other hand, the results from IonQ demonstrate an unexpected oscillated behavior, implying an intrinsic non-Markovian nature of the device.

The quantum channels considered in our work are pure dephasing. It will be interesting to generalize the present work to the cases of different channels, such as a depolarizing channel or amplitude damping channel. In addition, the quantum control can also be used in the case of indefinite causal order [76–80]. How the second demon affects the extractable work in this case also deserves further investigations.

### ACKNOWLEDGMENTS

We acknowledge the NTU-IBM Q Hub and Cloud Computing Center for Quantum Science & Technology at NCKU for providing us platforms to implement the circuits. The views expressed are those of the authors and do not reflect the official policy or position of IBM or the IBM Quantum Experience team. H.-Y.K. is supported by the National Center for Theoretical Sciences and National Science and Technology Council, Taiwan (Grants No. MOST 110-2811-M-006-546 and No. MOST 111-2917-I-564-005). H.-B.C. is supported by the National Science and Technology Council, Taiwan, Grant No. MOST 110-2112-M-006-012. This work is supported by the National Center for Theoretical Sciences and National Science and Technology Council, Taiwan, Grant No. MOST 111-2123-M-006-001.

### APPENDIX A: SEMIDEFINITE PROGRAM FOR THE CLASSICAL LIMITS OF AVERAGE EXTRACTED WORK

In this section we briefly summarize how to obtain the classical limit of the average extracted work by introducing the hidden-state (HS) model and semidefinite program (SDP). Bob will conceive that the assemblage  $\{p(a|x)\Lambda(\rho_{a|x})\}$  is classical whenever it can be decomposed with the HS model [23] as Eq. (6). If Bob can construct any one of such decompositions, he considers that the extracted work is produced by classical resources. Therefore, for a given work extraction protocol, consisting of  $\{F_{a|x}\}_{a|x}$  and the Gibbs state  $\rho_{\mathcal{V}}$ , the classical limit of average extracted work is the maximal value attainable by classical assemblages (described by the HS model). Besides, since all the marginals of the HS model should result in the same Gibbs state  $\rho_{\mathcal{V}}$ , as discussed in Sec. II, this imposes an additional constraint on the definition of the classical limit. Furthermore, because the set of all HS models (denoted as  $\mathcal{C}$ ) is a convex set, we can define the classical limit of average extracted work as a convex optimization problem, recalled from the main context:

$$\begin{aligned} \bar{W}_{\text{cl}} &= \max_{\{\tilde{\sigma}_{a|x}\} \in \mathcal{C}} \sum_{a,x} \text{Tr}[F_{a|x} \tilde{\sigma}_{a|x}], \\ \text{s.t. } \sum_a \tilde{\sigma}_{a|x} &= \rho_{\mathcal{V}} \quad \forall x. \end{aligned} \quad (\text{A1})$$

To solve the above optimization problem, we recast the HS model by introducing the deterministic strategy [24,25]. Let us consider  $x \in \{1, 2, \dots, m\}$  and  $a \in \{1, 2, \dots, q\}$ . Since  $m$  and  $q$  are finite, the number of hidden variables  $\lambda$  is  $q^m$ . Each  $\lambda$  can be considered as a string of ordered outcomes according to the measurements, i.e.,  $\lambda = (a_{x=1}, a_{x=2}, \dots, a_{x=m})$ . We can now define the deterministic strategy with  $\delta_{a,\lambda(x)}$ , where  $\delta$  is the Kronecker delta function and  $\lambda(x)$  denotes the value of  $a$  at position  $x$ . Therefore the HS model in Eq. (6) can be expressed by the deterministic strategy  $\delta_{a,\lambda(x)}$  together with a set of unnormalized hidden states  $\{\sigma_\lambda\}_\lambda$ , namely,  $\sigma_{a|x}^{\text{HS}} = \sum_\lambda \delta_{a,\lambda(x)} \sigma_\lambda$ . We can then recast the constraint in Eq. (A1) as

$$\begin{aligned} \sum_a \tilde{\sigma}_{a|x} &= \sum_{a,\lambda} \delta_{a,\lambda(x)} \sigma_\lambda = \sum_\lambda \sigma_\lambda = \rho_{\mathcal{V}} \quad \forall x \\ \text{and } \sigma_\lambda &\geq 0 \quad \forall \lambda. \end{aligned} \quad (\text{A2})$$

The second equality in the first constraint holds because  $\sum_a \delta_{a,\lambda(x)} = 1$  for all  $\lambda$  and  $x$ . Since  $\{\sigma_\lambda\}_\lambda$  belongs to a convex set and all the constraints are linear, one can obtain the optimal solution of Eq. (A1) by solving the following semidefinite program:

$$\begin{aligned} \bar{W}_{\text{cl}} &= \max_{\{\sigma_\lambda\}} \sum_{a,x,\lambda} \delta_{a,\lambda(x)} \text{Tr}[F_{a|x} \sigma_\lambda], \\ \text{s.t. } \sum_\lambda \sigma_\lambda &= \rho_{\mathcal{V}}, \\ \sigma_\lambda &\geq 0 \quad \forall \lambda. \end{aligned} \quad (\text{A3})$$

Finally, we obtain the value of the classical limit of average extracted work.

Here, we take the case summarized in Table I as an example and provide the optimal solution obtained from the SDP in Eq. (A3). Since  $x \in \{\sigma_x, \sigma_z\}$  and  $a \in \{+1, -1\}$ , the number of local hidden variables  $\lambda$  is 4, and each  $\lambda = (a_{x=\sigma_z}, a_{x=\sigma_x})$ . Therefore, by numerically solving the SDP in Eq. (A3), one can obtain the optimal value of  $\bar{W}_{\text{cl}} \approx 0.354 \hbar \omega$ , where the hidden variable  $\lambda$  and the optimal solution  $\{\sigma_\lambda^*\}$  can be summarized in Table IV. Furthermore, one can obtain the optimal

TABLE IV. One of the optimal solutions of Eq. (A3) for the case summarized in Table I. Each  $\lambda$  can be considered as a string of ordered outcomes according to the measurements. Here,  $\sigma_\lambda^*$  denotes the optimal solution for the un-normalized hidden states obtained from the SDP.

| $\lambda = (a_{x=\sigma_z}, a_{x=\sigma_x})$ | $\sigma_\lambda^*$   |
|--|--|
| (+1, +1)                                     | $\begin{pmatrix} 0.2134 & 0.0884 \\ 0.0884 & 0.0366 \end{pmatrix}$   |
| (+1, -1)                                     | $\begin{pmatrix} 0.2134 & -0.0884 \\ -0.0884 & 0.0366 \end{pmatrix}$ |
| (-1, +1)                                     | $\begin{pmatrix} 0.0366 & 0.0884 \\ 0.00884 & 0.2134 \end{pmatrix}$  |
| (-1, -1)                                     | $\begin{pmatrix} 0.0366 & -0.0884 \\ -0.0884 & 0.2134 \end{pmatrix}$ |



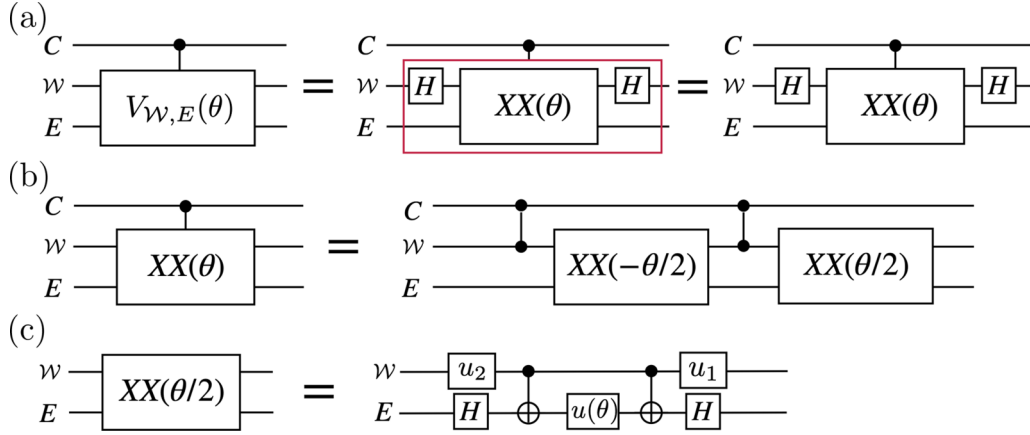


FIG. 7. (a) The controlled  $V_{W,E}$  can be decomposed into two  $H$  gates and a controlled- $XX(\theta)$  gate. (b) Controlled  $XX(\theta)$  can be decomposed to the combination of two controlled- $Z$  gates,  $XX(-\theta/2)$  and  $XX(\theta/2)$ . (c) The decompositions of  $XX(\theta)$  are  $u_1$ ,  $u_2$ ,  $u(\theta)$ , two  $H$  gates, two CNOT gates, and  $H$  gates.

HS assemblage:

$$\begin{aligned}
 \sigma_{a=+1|x=\sigma_z}^{\text{HS}} &\approx \begin{pmatrix} 0.4268 & 0.0000 \\ 0.0000 & 0.0732 \end{pmatrix}, \\
 \sigma_{a=-1|x=\sigma_z}^{\text{HS}} &\approx \begin{pmatrix} 0.0732 & 0.0000 \\ 0.0000 & 0.4268 \end{pmatrix}, \\
 \sigma_{a=+1|x=\sigma_x}^{\text{HS}} &\approx \begin{pmatrix} 0.2500 & 0.1768 \\ 0.1768 & 0.2500 \end{pmatrix}, \\
 \sigma_{a=-1|x=\sigma_x}^{\text{HS}} &\approx \begin{pmatrix} 0.2500 & -0.1768 \\ -0.1768 & 0.2500 \end{pmatrix}. \quad (\text{A4})
 \end{aligned}$$

Note that the optimal solution  $\{\sigma_\lambda^*\}$  is not unique, and the above HS assemblage is therefore not unique either.

## APPENDIX B: THE DECOMPOSITION OF CONTROLLED- $V_{W,E}$ OPERATIONS

In this section we describe in detail how we decompose the controlled  $V_{W,E}$  into the combination of two-qubit gates and single-qubit gates that can be applied on IBMQ and IonQ platforms.

According to Eq. (9), we can construct the  $V_{W,E}(\theta)$  as

$$V_{W,E}(\theta) = \begin{pmatrix} \cos(\frac{\theta}{2}) & -i \sin(\frac{\theta}{2}) & 0 & 0 \\ -i \sin(\frac{\theta}{2}) & \cos(\frac{\theta}{2}) & 0 & 0 \\ 0 & 0 & \cos(\frac{\theta}{2}) & i \sin(\frac{\theta}{2}) \\ 0 & 0 & i \sin(\frac{\theta}{2}) & \cos(\frac{\theta}{2}) \end{pmatrix}. \quad (\text{B1})$$

In addition, to achieve the superposition of quantum channels, we use a controlled unitary according to Eq. (10). Moreover, the controlled unitary is equal to the product of two controlled unitaries.

We now consider the controlled unitary:  $|0\rangle\langle 0|_C \otimes \mathbb{1} + |1\rangle\langle 1|_C \otimes V_{W,E}$ , as shown in Fig. 7(a). From Eq. (B1),  $V_{W,E}$  is equal to  $(H \otimes \mathbb{1})XX(\theta)(H \otimes \mathbb{1})$ , where  $XX(\theta)$  is a kind of Ising coupling gate denoted as  $XX(\theta) = \cos(\theta/2)\mathbb{1} \otimes \mathbb{1} - i \sin(\theta/2)\sigma_x \otimes \sigma_x$ . The controlled  $V_{W,E}$  can be separated to three controlled unitaries: two controlled- $H$  operations and a controlled- $XX(\theta)$  operation. In this case the two controlled- $H$  operations can be replaced with two  $H$  gates applied to the  $W$ . Thus we can focus on the  $XX(\theta)$ . As shown in Fig. 7(b), the controlled  $XX(\theta)$  can be decomposed to two controlled- $Z$  operations,  $XX(-\theta/2)$  and  $XX(\theta/2)$ .

However, IBMQ does not have the Ising coupling gates. According to IBMQ,  $XX(\theta)$  can be decomposed to  $u_1$ ,  $u_2$ ,  $u(\theta)$ , two  $H$ s, and two CNOT operations. In Fig. 7(c), we show the order of the aforementioned unitary operations to construct the  $XX(\theta)$ .

- [1] M. O. Scully, K. R. Chapin, K. E. Dorfman, M. B. Kim, and A. Svidzinsky, Quantum heat engine power can be increased by noise-induced coherence, *Proc. Natl. Acad. Sci. USA* **108**, 15097 (2011).
- [2] S. Rahav, U. Harbola, and S. Mukamel, Heat fluctuations and coherences in a quantum heat engine, *Phys. Rev. A* **86**, 043843 (2012).

- [3] N. Brunner, M. Huber, N. Linden, S. Popescu, R. Silva, and P. Skrzypczyk, Entanglement enhances cooling in microscopic quantum refrigerators, *Phys. Rev. E* **89**, 032115 (2014).
- [4] M. T. Mitchison, M. P. Woods, J. Prior, and M. Huber, Coherence-assisted single-shot cooling by quantum absorption refrigerators, *New J. Phys.* **17**, 115013 (2015).

- [5] H.-B. Chen, P.-Y. Chiu, and Y.-N. Chen, Vibration-induced coherence enhancement of the performance of a biological quantum heat engine, *Phys. Rev. E* **94**, 052101 (2016).
- [6] K. Brandner, M. Bauer, and U. Seifert, Universal Coherence-Induced Power Losses of Quantum Heat Engines in Linear Response, *Phys. Rev. Lett.* **119**, 170602 (2017).
- [7] G. Manzano, F. Plastina, and R. Zambrini, Optimal Work Extraction and Thermodynamics of Quantum Measurements and Correlations, *Phys. Rev. Lett.* **121**, 120602 (2018).
- [8] M. P. Woods, N. H. Y. Ng, and S. Wehner, The maximum efficiency of nano heat engines depends on more than temperature, *Quantum* **3**, 177 (2019).
- [9] W. Niedenzu, M. Huber, and E. Boukobza, Concepts of work in autonomous quantum heat engines, *Quantum* **3**, 195 (2019).
- [10] N. V. Horne, D. Yum, T. Dutta, P. Hänggi, J. Gong, D. Poletti, and M. Mukherjee, Single-atom energy-conversion device with a quantum load, *npj Quantum Inf.* **6**, 37 (2020).
- [11] M. Gluza, J. Sabino, N. H. Y. Ng, G. Vitagliano, M. Pezzutto, Y. Omar, I. Mazets, M. Huber, J. Schmiedmayer, and J. Eisert, Quantum field thermal machines, *PRX Quantum* **2**, 030310 (2021).
- [12] J. Son, P. Talkner, and J. Thingna, Monitoring quantum Otto engines, *PRX Quantum* **2**, 040328 (2021).
- [13] Y. Lu, N. Lambert, A. F. Kockum, K. Funo, A. Bengtsson, S. Gasparinetti, F. Nori, and P. Delsing, Steady-state heat transport and work with a single artificial atom coupled to a waveguide: Emission without external driving, *PRX Quantum* **3**, 020305 (2022).
- [14] K. Funo, Y. Watanabe, and M. Ueda, Thermodynamic work gain from entanglement, *Phys. Rev. A* **88**, 052319 (2013).
- [15] P. Skrzypczyk, A. J. Short, and S. Popescu, Work extraction and thermodynamics for individual quantum systems, *Nat. Commun.* **5**, 4185 (2014).
- [16] A. M. Alhambra, L. Masanes, J. Oppenheim, and C. Perry, Fluctuating Work: From Quantum Thermodynamical Identities to a Second Law Equality, *Phys. Rev. X* **6**, 041017 (2016).
- [17] C. Elouard, D. Herrera-Martí, B. Huard, and A. Auffèves, Extracting Work from Quantum Measurement in Maxwell's Demon Engines, *Phys. Rev. Lett.* **118**, 260603 (2017).
- [18] B. Morris, L. Lami, and G. Adesso, Assisted Work Distillation, *Phys. Rev. Lett.* **122**, 130601 (2019).
- [19] A. E. Allahverdyan, Nonequilibrium quantum fluctuations of work, *Phys. Rev. E* **90**, 032137 (2014).
- [20] P. Talkner and P. Hänggi, Aspects of quantum work, *Phys. Rev. E* **93**, 022131 (2016).
- [21] M. Lostaglio, Á. M. Alhambra, and C. Perry, Elementary thermal operations, *Quantum* **2**, 52 (2018).
- [22] E. Schrödinger, Discussion of probability relations between separated systems, *Math. Proc. Cambridge Philos. Soc.* **31**, 555 (1935).
- [23] H. M. Wiseman, S. J. Jones, and A. C. Doherty, Steering, Entanglement, Nonlocality, and the Einstein-Podolsky-Rosen Paradox, *Phys. Rev. Lett.* **98**, 140402 (2007).
- [24] D. Cavalcanti and P. Skrzypczyk, Quantum steering: A review with focus on semidefinite programming, *Rep. Prog. Phys.* **80**, 024001 (2017).
- [25] R. Uola, A. C. S. Costa, H. C. Nguyen, and O. Gühne, Quantum steering, *Rev. Mod. Phys.* **92**, 015001 (2020).
- [26] Y. Xiang, S. Cheng, Q. Gong, Z. Ficek, and Q. He, Quantum steering: Practical challenges and future directions, *PRX Quantum* **3**, 030102 (2022).
- [27] K. Beyer, K. Luoma, and W. T. Strunz, Steering Heat Engines: A Truly Quantum Maxwell Demon, *Phys. Rev. Lett.* **123**, 250606 (2019).
- [28] W. Ji, Z. Chai, M. Wang, Y. Guo, X. Rong, F. Shi, C. Ren, Y. Wang, and J. Du, Spin Quantum Heat Engine Quantified by Quantum Steering, *Phys. Rev. Lett.* **128**, 090602 (2022).
- [29] C. G. Knott, *The Life and Scientific Work of Peter Guthrie Tait* (Cambridge University Press, Cambridge, 1911).
- [30] A. J. Leggett and A. Garg, Quantum Mechanics Versus Macroscopic Realism: Is the Flux There When Nobody Looks? *Phys. Rev. Lett.* **54**, 857 (1985).
- [31] K. Joarder, D. Saha, D. Home, and U. Sinha, Loophole-free interferometric test of macrorealism using heralded single photons, *PRX Quantum* **3**, 010307 (2022).
- [32] C. Emary, N. Lambert, and F. Nori, Leggett-Garg inequalities, *Rep. Prog. Phys.* **77**, 016001 (2014).
- [33] H.-Y. Ku, J. Kadlec, A. Černoč, M. T. Quintino, W. Zhou, K. Lemr, N. Lambert, A. Miranowicz, S.-L. Chen, F. Nori, and Y.-N. Chen, Quantifying quantumness of channels without entanglement, *PRX Quantum* **3**, 020338 (2022).
- [34] L. B. Vieira and C. Budroni, Temporal correlations in the simplest measurement sequences, *Quantum* **6**, 623 (2022).
- [35] A. G. Maity, S. Mal, C. Jebarathinam, and A. S. Majumdar, Self-testing of binary pauli measurements requiring neither entanglement nor any dimensional restriction, *Phys. Rev. A* **103**, 062604 (2021).
- [36] Y.-N. Chen, C.-M. Li, N. Lambert, S.-L. Chen, Y. Ota, G.-Y. Chen, and F. Nori, Temporal steering inequality, *Phys. Rev. A* **89**, 032112 (2014).
- [37] C.-M. Li, Y.-N. Chen, N. Lambert, C.-Y. Chiu, and F. Nori, Certifying single-system steering for quantum-information processing, *Phys. Rev. A* **92**, 062310 (2015).
- [38] S.-L. Chen, N. Lambert, C.-M. Li, A. Miranowicz, Y.-N. Chen, and F. Nori, Quantifying Non-Markovianity with Temporal Steering, *Phys. Rev. Lett.* **116**, 020503 (2016).
- [39] H.-Y. Ku, S.-L. Chen, N. Lambert, Y.-N. Chen, and F. Nori, Hierarchy in temporal quantum correlations, *Phys. Rev. A* **98**, 022104 (2018).
- [40] J.-D. Lin, W.-Y. Lin, H.-Y. Ku, N. Lambert, Y.-N. Chen, and F. Nori, Quantum steering as a witness of quantum scrambling, *Phys. Rev. A* **104**, 022614 (2021).
- [41] P. A. Guérin, A. Feix, M. Araújo, and Č. Brukner, Exponential Communication Complexity Advantage from Quantum Superposition of the Direction of Communication, *Phys. Rev. Lett.* **117**, 100502 (2016).
- [42] G. Chiribella and H. Kristjánsson, Quantum Shannon theory with superpositions of trajectories, *Proc. R. Soc. London, Ser. A* **475**, 20180903 (2019).
- [43] A. A. Abbott, J. Wechs, D. Horsman, M. Mhalla, and C. Branciard, Communication through coherent control of quantum channels, *Quantum* **4**, 333 (2020).
- [44] H. Kristjánsson, G. Chiribella, S. Salek, D. Ebler, and M. Wilson, Resource theories of communication, *New J. Phys.* **22**, 073014 (2020).

- [45] M. Ban, Two-qubit correlation in two independent environments with indefiniteness, *Phys. Lett. A* **385**, 126936 (2021).
- [46] G. Rubino, L. A. Rozema, D. Ebler, H. Kristjánsson, S. Salek, P. Allard Guérin, Č. Brukner, A. A. Abbott, C. Branciard, G. Chiribella, and P. Walther, Experimental quantum communication enhancement by superposing trajectories, *Phys. Rev. Res.* **3**, 013093 (2021).
- [47] J.-D. Lin, C.-Y. Huang, N. Lambert, G.-Y. Chen, F. Nori, and Y.-N. Chen, Space-time dual quantum zeno effect: Interferometric engineering of open quantum system dynamics, *Phys. Rev. Res.* **4**, 033143 (2022).
- [48] K.-Y. Lee, J.-D. Lin, A. Miranowicz, F. Nori, H.-Y. Ku, and Y.-N. Chen, Steering-enhanced quantum metrology using superpositions of quantum channels, [arXiv:2206.03760](https://arxiv.org/abs/2206.03760).
- [49] IBM Quantum Services, <https://quantum-computing.ibm.com/services?services=systems&system>, [May. 2022].
- [50] C. Berke, E. Varvelis, S. Trebst, A. Altland, and D. P. DiVincenzo, Transmon platform for quantum computing challenged by chaotic fluctuations, *Nat. Commun.* **13**, 2495 (2022).
- [51] A. Strikis, D. Qin, Y. Chen, S. C. Benjamin, and Y. Li, Learning-based quantum error mitigation, *PRX Quantum* **2**, 040330 (2021).
- [52] I. Pogorelov, T. Feldker, C. D. Marciniak, L. Postler, G. Jacob, O. Kriegelsteiner, V. Podlesnic, M. Meth, V. Negnevitsky, M. Stadler, B. Höfer, C. Wächter, K. Lakhmanskiy, R. Blatt, P. Schindler, and T. Monz, Compact ion-trap quantum computing demonstrator, *PRX Quantum* **2**, 020343 (2021).
- [53] C. Branciard, E. G. Cavalcanti, S. P. Walborn, V. Scarani, and H. M. Wiseman, One-sided device-independent quantum key distribution: Security, feasibility, and the connection with steering, *Phys. Rev. A* **85**, 010301(R) (2012).
- [54] B. Yadin, M. Fadel, and M. Gessner, Metrological complementarity reveals the Einstein-Podolsky-Rosen paradox, *Nat. Commun.* **12**, 2410 (2021).
- [55] Y.-Y. Zhao, H.-Y. Ku, S.-L. Chen, H.-B. Chen, F. Nori, G.-Y. Xiang, C.-F. Li, G.-C. Guo, and Y.-N. Chen, Experimental demonstration of measurement-device-independent measure of quantum steering, *npj Quantum Inf.* **6**, 77 (2020).
- [56] S. Slussarenko, D. J. Joch, N. Tischler, F. Ghafari, L. K. Shalm, V. B. Verma, S. W. Nam, and G. J. Pryde, Quantum steering with vector vortex photon states with the detection loophole closed, *npj Quantum Inf.* **8**, 20 (2022).
- [57] D. Janzing, Thermodynamic cost of reliability and low temperatures: Tightening Landauer's principle and the second law, *Int. J. Theor. Phys.* **39**, 2717 (2000).
- [58] P. Faist, J. Oppenheim, and R. Renner, Gibbs-preserving maps outperform thermal operations in the quantum regime, *New J. Phys.* **17**, 043003 (2015).
- [59] P. Faist, F. Dupuis, J. Oppenheim, and R. Renner, The minimal work cost of information processing, *Nat. Commun.* **6**, 7669 (2015).
- [60] M. Lostaglio, An introductory review of the resource theory approach to thermodynamics, *Rep. Prog. Phys.* **82**, 114001 (2019).
- [61] C.-Y. Hsieh, Communication, dynamical resource theory, and thermodynamics, *PRX Quantum* **2**, 020318 (2021).
- [62] G. Sagnol and M. Stahlberg, PICOS: A Python interface to conic optimization solvers, *J. Open Source Software* **7**, 3915 (2022).
- [63] W. F. Stinespring, Positive functions on  $C^*$ -algebras, *Proc. Am. Math. Soc.* **6**, 211 (1955).
- [64] *States, Effects, and Operations Fundamental Notions of Quantum Theory*, edited by K. Kraus, A. Böhm, J. D. Dollard, and W. H. Wootters (Springer Berlin, Heidelberg, 1983).
- [65] M. M. Wilde, Preface to the second edition, in *Quantum Information Theory* (Cambridge University Press, Cambridge, 2017), pp. xi–xii.
- [66] R. Gallego and L. Aolita, Resource Theory of Steering, *Phys. Rev. X* **5**, 041008 (2015).
- [67] R. V. Nery, M. M. Taddei, P. Sahium, S. P. Walborn, L. Aolita, and G. H. Aguilar, Distillation of Quantum Steering, *Phys. Rev. Lett.* **124**, 120402 (2020).
- [68] S. Gupta, D. Das, and A. S. Majumdar, Distillation of genuine tripartite Einstein-Podolsky-Rosen steering, *Phys. Rev. A* **104**, 022409 (2021).
- [69] H.-Y. Ku, C.-Y. Hsieh, S.-L. Chen, Y.-N. Chen, and C. Budroni, Complete classification of steerability under local filters and its relation with measurement incompatibility, *Nat. Commun.* **13**, 4973 (2022).
- [70] H.-Y. Ku, N. Lambert, F.-J. Chan, C. Emary, Y.-N. Chen, and F. Nori, Experimental test of non-macrorealistic cat states in the cloud, *npj Quantum Inf.* **6**, 98 (2020).
- [71] Y.-T. Huang, J.-D. Lin, H.-Y. Ku, and Y.-N. Chen, Benchmarking quantum state transfer on quantum devices, *Phys. Rev. Res.* **3**, 023038 (2021).
- [72] E. Magesan, J. M. Gambetta, and J. Emerson, Scalable and Robust Randomized Benchmarking of Quantum Processes, *Phys. Rev. Lett.* **106**, 180504 (2011).
- [73] E. Magesan, J. M. Gambetta, and J. Emerson, Characterizing quantum gates via randomized benchmarking, *Phys. Rev. A* **85**, 042311 (2012).
- [74] M. Urbanek, B. Nachman, V. R. Pascuzzi, A. He, C. W. Bauer, and W. A. de Jong, Mitigating Depolarizing Noise on Quantum Computers with Noise-Estimation Circuits, *Phys. Rev. Lett.* **127**, 270502 (2021).
- [75] P. Figueroa-Romero, K. Modi, R. J. Harris, T. M. Stace, and M.-H. Hsieh, Randomized benchmarking for non-Markovian noise, *PRX Quantum* **2**, 040351 (2021).
- [76] D. Ebler, S. Salek, and G. Chiribella, Enhanced Communication with the Assistance of Indefinite Causal Order, *Phys. Rev. Lett.* **120**, 120502 (2018).
- [77] N. Loizeau and A. Grinbaum, Channel capacity enhancement with indefinite causal order, *Phys. Rev. A* **101**, 012340 (2020).
- [78] D. Felce and V. Vedral, Quantum Refrigeration with Indefinite Causal Order, *Phys. Rev. Lett.* **125**, 070603 (2020).
- [79] T. Guha, M. Alimuddin, and P. Parashar, Thermodynamic advancement in the causally inseparable occurrence of thermal maps, *Phys. Rev. A* **102**, 032215 (2020).
- [80] K. Simonov, G. Francica, G. Guarnieri, and M. Paternostro, Work extraction from coherently activated maps via quantum switch, *Phys. Rev. A* **105**, 032217 (2022).